Applied Catalysis B: Environmental 263 (2020) 118345

Contents lists available at ScienceDirect

Applied Catalysis B: Environmental

journal homepage: www.elsevier.com/locate/apcatb

Engineering PtRu bimetallic nanoparticles with adjustable alloying degree for methanol electrooxidation: Enhanced catalytic performance

Junming Zhang, Ximing Qu, Yu Han, Linfan Shen, Shuhu Yin, Guang Li, Yanxia Jiang*, Shigang Sun*

State Key Laboratory of Physical Chemistry of Solid Surfaces, Department of Chemistry, College of Chemistry and Chemical Engineering, Xiamen University, Xiamen, 361005, People's Republic of China

ARTICLE INFO

Keywords:
PtRu alloy
Porous graphitic carbon
Thermal treatment
Methanol oxidation
In-situ FTIRS

ABSTRACT

PtRu bimetal is of particularly attractive in various electrocatalytic reactions owing to its synergistic effect, ligand effect and strain effect. Here, PtRu nanoalloy supported on porous graphitic carbon (PC) has been successfully prepared via a very facile method involving co-reduction the precursors of Pt and Ru at 300 °C by H_2 (PtRu/PC−L) followed by thermal treatment at high temperature (700 °C, PtRu/PC–H). Specifically, the electrocatalytic performance of PtRu/PC nanoalloy could be dramatically enhanced through high-temperature annealing. This strategy has synthesized smaller Pt and PtRu nanoparticles (ca. < 3 nm); what's more, they are all homogeneous deposited on the surface of PC. PtRu/PC–H nanocatalyst displays higher alloying degree and stronger electronic interaction between Pt and Ru atoms accompanied by the downshift of Pt d-band center. Studies of electrochemical tests indicate that the as-fabricated PtRu/PC–H sample exhibits superior electrocatalytic performance and excellent CO-poisoning tolerance compared with PtRu/PC−L and Pt/PC nanocatalysts. The mass activity and specific activity on PtRu/PC–H nanoalloy can be increased to 1674.2 mA mg_{Pt}^{-1} and 4.4 mA cm^{-2} for MOR, it is 4.08 and 8.80 times higher than that of the Pt/PC nanocatalyst, respectively. From in-situ FTIR spectra, we can discover PtRu/PC–H nanoalloy generates CO_2 at a lower potential of −150 mV than those on PtRu/PC–L (0 mV) and Pt/PC (50 mV) nanocatalysts, dramatically improves the ability of cleavage C–H bond and alleviates the CO_{ads} poisoning on active sites. The PtRu/PC−H nanocatalyst exhibits maximum power density of 83.7 mW cm^{-2} in single methanol fuel cell test, which more than threefold than that of commercial Pt/C as the anode catalyst. Those experimental results open an effective and clean avenue in the development and preparation of high-performance Pt-based nanocatalysts for direct methanol fuel cells.

1. Introduction

Direct methanol fuel cells (DMFCs) are sustainable and eco-friendly candidates to work as high-efficiency power sources because of their relatively high energy density (6.1 kW h kg^{-1}), environmental friendliness and simple fabrication procedure [1–6]. However, it is still challenging to realize the mass commercialization, mainly originating from the arduous task of developing high-efficiency and economical electrocatalysts to reduce the over-potential and mitigate the slow kinetics of anodic methanol oxidation [7–10]. Noble metal Platinum possesses the stronger ability of cleavage C–H bond among all the pure metals, so that it has been widely identified as the state-of-the-art catalyst for some small organic molecules oxidation reactions (MOR, EOR, etc.) [11,12]. In consideration of high cost and scarcity, reducing the Pt loading of as-prepared catalyst is an essential approach for achieving the commercialization of DMFCs. Moreover, the intermediate species, carbon monoxide, is known to easily contaminate Pt active sites by strongly adsorbing and inhibit catalytic functions. As a result, binary Pt-based nanocatalysts have been widely prepared such as PtRu, PtCu, PtFe, PtSn, PtZn, PtPb and PtMo etc., which maximize the utilization efficiency of Pt, adjust the electronic structure of active sites, change the chemical properties of metal atoms, and enhance the electrocatalytic performance for MOR [13–19]. Previous studies suggested that the addition of a second metal could provide more sites to absorb oxygenated species, facilitate the oxidative removal of CO_{ads} at lower potentials, and significantly weaken the adsorption of intermediates on Pt surface [20,21]. For instance, Kwon et al. synthesized three kinds of Pt-based nanoparticles (PtMn, PtFe and PtCo) via sonochemical reactions and investigated their electrocatalytic properties for MOR [8]. They found the incorporation of transition metals in Pt atoms could

* Corresponding authors.
E-mail addresses: yxjiang@xmu.edu.cn (Y. Jiang), sgsun@xmu.edu.cn (S. Sun).

https://doi.org/10.1016/j.apcatb.2019.118345
Received 12 August 2019; Received in revised form 18 October 2019; Accepted 26 October 2019
Available online 04 November 2019
0926-3373/ © 2019 Elsevier B.V. All rights reserved.

effectively enhance MOR performance, PtFe and PtCo with transition-metal-content 39.0 at% and 46.6 at%, respectively, showed 2–3 fold enhancement in mass and specific activity compared with commercial Pt/C. As another example, Wang's group prepared porous flower-like $Pt_{72}Ru_{28}$ nanoalloys assembled with sub-4.0 nm nanoparticles, the specific and mass activity is 10.98 mA cm^{-2} and 1700 mA mg_{Pt}^{-1} for MOR, respectively, which are 4.19 and 3.54 times than that of commercial Pt black [21]. Improved catalytic activity was ascribed to the modification of Pt electronic structure and Ru chemical properties in nanoparticles surface by the strain and ligand effects.

On account of the synergistic effect, ligand effect and strain effect, bimetallic Pt-based nanocatalysts often exhibit enhanced catalytic properties than their mono-component counterparts for MOR. In particular, among various binary nanocatalysts, PtRu is deemed to the most promising bimetallic catalyst in DMFCs [22]. In comparison with Pt, the oxygenated species of Ru surface could appear at a lower oxidation potential (0.35 V vs. RHE), and alloying Pt with Ru affords favorable alteration for the electronic structure of Pt [23]. Therefore, the famous “bifunctional mechanism” has been proposed for PtRu nanocatalysts, Pt sites can cleave the C–H bond of methanol molecule and adsorb CO, the neighboring Ru atoms can activate water and provide more oxygen-containing species to remove the poisoning intermediate on adjacent Pt active sites. Many works about PtRu nanocatalysts have been reported, which showed it is the best binary nanocatalyst for MOR, and recently develop some novel PtRu nanocatalysts with different electro-structures and morphology. For example, Xing and coworkers synthesized a Pt_xRu_y nanosponge, and the Ru-enriched Pt_1Ru_3 catalyst had higher MOR performance. With the increasing of Ru contents, the surface electronic structure of Pt was obviously improved [24]. Yang et al. reported the synthesis of Ru decorated Pt bimetallic cubes and icosahedra, the specific and mass activity of Ru decorated Pt bimetallic icosahedra is 6.7 and 2.2 times higher than that of Pt_7Ru/C nanoparticles, respectively [25]. Dong et al. prepared three kinds of morphologies PtRu nanocrystals (nanowires, nanorods, and nanocubes) and evaluated the relation between facets and electrocatalytic performance for MOR. The mass activity of {111}-terminated nanowires was 2.28 and 4.32 times higher than those of {100}-terminated PtRu nanocubes and commercial Pt/C, respectively [26]. Since the catalytic activity depends strongly on the preparation or treated methods, followed by generating various atomic structures and different degree of alloying on the alloy nanoparticles [27,28]. Moreover, Yang and Cen reported that 1:1 was the optimum atom ratio for PtRu nanoparticles in methanol electrocatalytic reactions [29,30], and a simple and effective strategy was needed. According to the above description, here, we adopt a facile and clean thermal treatment method to synthesize high alloying degree PtRu/PC–H nanocatalyst, the mass activity for MOR is higher and limited reports beyond the value in similar acidic medium. In addition, this is the first time to enhance the electrocatalytic performance of nanoalloy via high-temperature treatment in the PtRu system.

The efficient operation of DMFCs requires complete oxidation of methanol to CO_2 at lower potentials. For MOR on Pt-based, a range of adsorbed intermediates appears in the reaction process, so that the electrooxidation mechanism still is complex. For example, Li's group prepared a tensile-strained Pt_3Ga intermetallic with two-to-three Pt atomic-layer as an active electrocatalyst for MOR [31]. They carried out density functional theory (DFT) calculations to investigate many possible reaction routes of MOR and definite value of reaction free energy (ΔG) was calculated in their work, indicating the dehydrogenation of methanol is much easier to C–H bond compared to O—H bond in complex MOR process. As we all know, methanol can be oxidated via parallel duel pathways to CO_2, namely, direct formaldehyde and formic acid paths and indirect CO poisoning paths [32,33]. Studies through electrochemical methods and in situ FTIR spectroscopy indicate that adsorption of methanol molecule and subsequent dehydrogenation is hindered when the CO surface abundance reaches 30% of a monolayer [34]. Thus for MOR, the catalyst design challenge involves the minimization of CO surface concentration and/or its rapid removal at the lowest possible overpotential.

In this work, we proposed a facile and clean thermal treatment strategy for controllable synthesis of PtRu/PC–H nanocatalyst with a high alloying degree and the as-prepared nanoalloy was used as high-efficient MOR nanocatalysts. The nanostructures of as-synthesized catalysts were characterized by X-ray diffraction (XRD), Energy dispersive X-ray (EDX), transmission electron microscopy (TEM) and X-ray photoelectron spectroscopy (XPS). The PtRu nanoparticles with smaller size were highly uniform supported on PC. Electrochemical tests illustrated that the as-synthesized PtRu/PC–H nanoalloy versus PtRu/PC-L and Pt/PC displayed 2.25/1.42 and 4.08/8.80-fold enhancement of mass activity and specific activity toward MOR, respectively. In-situ FTIR spectra implied that PtRu/PC–H nanoalloys were more easy to remove the CO_{ads} than those PtRu/PC-L and Pt/PC nanocatalysts. Here, we report the correlation from an investigation of the relationship between high-temperature thermal treatment of PtRu nanocatalysts and their MOR activity.

2. Experimental section

2.1. Chemicals and materials

$H_2PtCl_6{\cdot}6H_2O$, $RuCl_3{\cdot}3H_2O$, methanol, perchloric acid, ethanol, nitric acid and hydrochloric acid were obtained from Sinopharm Chemical Reagent Co. Ltd. (Shanghai, China). A 5 wt% Nafion solution was purchased from Sigma-Aldrich. All gases were obtained from Linde Co. (Xiamen, China). All of the chemical reagents are of analytical grade and used as received without any further purification. The solutions throughout the electrochemical experiments were prepared using Millipore water (18.2 MΩ cm).

2.2. Synthesis of nanocatalysts

Porous graphitic carbon was prepared according to a method described previously of our group [35,36]. Nanocatalysts were synthesized as follows. First, 20 mg PC was added into 20 mL water, followed by ultrasonication for around 0.5 h to make sure the PC evenly dispersed into water. Second, the precursors of $H_2PtCl_6{\cdot}6H_2O$ (875 μL of 19.3 mM H_2PtCl_6) and $RuCl_3{\cdot}3H_2O$ (351 μL of 48.2 mM $RuCl_3$) were dispersed into above PC suspension liquid in an ultrasonic bath about 30 min again. Afterwards, the well-dispersed suspension was transferred to a water bath of 50 °C and kept continuous stirring before the solvents were evaporated. Then the resulting black sample was dried at 60 °C for 12 h in a vacuum oven. Immediately following, the dry sample was treated in a tube furnace under hydrogen at 300 °C for 3 h. Finally, the as-prepared product was washed and centrifuged repeatedly with water to remove the ions possibly remaining in final samples, and then dried at 60 °C for 12 h in a vacuum oven (denoted as PtRu/PC—L). Then as-prepared PtRu/PC—L nanocatalyst was continued to anneal 3 h in hydrogen at 700 °C (denoted as PtRu/PC–H), which 700 °C is the optimum annealing temperature to obtain best MOR catalyst (Fig. S1). As a comparison, Pt and Ru nanoparticles supported on PC were also prepared with a similar procedure as described above under hydrogen at 300 °C for 3 h (denoted as Pt/PC and Ru/PC). The total metal loading of four nanocatalysts was all kept consistent at 20 wt%.

2.3. Catalysts characterization

X-ray diffraction (XRD) measurements of as-prepared PC-supported Pt and PtRu nanocatalysts were taken on an X-ray Rigaku Dmax-3C diffractometer, with Cu Kα radiation source (λ = 1.5408 Å) at 40 kV and 30 mA. Energy dispersive X-ray (EDX) of samples was collected on a scanning electron microscopy (Hitachi S-4800 SEM). The morphologies and sizes of Pt/PC and PtRu/PC nanocatalysts were investigated

using a transmission electron microscope (TEM) and high-resolution TEM (HR-TEM, TECNAI F20) at 200 kV. For the measurements, the catalysts were diluted in ethanol and drop cast onto carbon-coated copper grids, then the solvent was evaporated at room temperature. The size of the as-prepared nanoparticles was measured from 200 nanoparticles in TEM images. X-ray photoelectron spectroscopy (XPS) measurements were carried out using a PHI Quantum 2000 with an Al Kα monochromatic X-ray source operating at 15 kV, and all of the electron binding energy was calibrated relative to the C1s peak at 284.6 eV. The content of Pt and Ru were determined by an inductively coupled plasma-optical emission spectrophotometer (ICP-OES, Thermo Electron IRIS Intrepid II XSP, USA). The samples were firstly dissolved with aqua regia, and then PC was eliminated by adding $HClO_4$ in a heat solution prudently. The Pt content of as-prepared Pt/PC, PtRu/PC-L and PtRu/PC–H nanocatalysts were determined to be 21.1%, 13.8% and 12.9%, respectively.

2.4. Electrochemical characterization

Electrochemical measurements were performed on PAR 263A potentiostat (EG&G) with a standard three-electrode cell, using platinum foil and saturated calomel electrode (SCE) as counter and the reference electrode, respectively. The working electrode was a catalyst-modified glassy carbon electrode of 5 mm diameter, coated with a total metal loading amount of 2 μg. The highly dispersed catalyst slurry was prepared as follows, 3 mg of as-prepared nanocatalyst was dispersed into a mixture of 5 wt% Nafion, water and isopropanol (v/v/v = 0.1/1/9) for 30 min in an ultrasonic bath. The readout currents were recorded with iR drop (ohmic drop caused by solution resistance) correction during the measurements. The electrochemical active surface area (ECSA) was calculated by integrating the charges associated with hydrogen regions on cyclic voltammetric (CV) in nitrogen-saturated 0.1 M $HClO_4$, and the potential was scanned between −0.27 and 1.00 V at a scan rate of 50 mV s^{-1}. Methanol electrooxidation measurements, the electrodes were cycled in 0.5 M methanol + 0.1 M $HClO_4$ solution. For CO-stripping voltammetry experiments, CO adsorption was conducted at −0.2 V for 10 min, and subsequently purged with N_2 for 20 min to remove the CO dissolved in the electrolyte. Whereafter, CO oxidation was executed in the potential window of −0.27–1.00 V at a rate of 50 mV s^{-1} for two cycles. The stability tests were evaluated by chronoamperometry and performed at 0.5 V with a scan rate of 50 mV s^{-1} and 7200 s.

Subsequently, the MOR oxidation test was achieved using in-situ FTIRS. It is an important means to investigate the electrocatalytic pathways and mechanism, benefit to guide the design of high-efficiency electrocatalysts. Electrochemical in situ FTIR measurements were carried out on a Nicolet 870 FTIR spectrometer equipped with a liquid-nitrogen-cooled MCT-A detector and an EverGlo IR source. A CaF_2 disk was used as the IR window, and an IR cell with a thin layer configuration between the electrode and the IR window was approached by pushing the electrode against the window before FTIR measurement [37]. During the FTIR measurement course, unpolarized IR radiation was passed through the window and solution thin layer (~ 10 μm), then it was reflected on the electrode surface. In situ FTIR spectra were collected using both single potential alteration FTIR spectroscopy (SPAFTIRS) and multi-stepped FTIR spectroscopy (MSFTIR) procedures. The reference spectrum at −0.27 V was acquired and used as the reference spectrum ($R(E_R)$). The sample spectrum ($R(E_S)$) was recorded in the potential range from −0.25 to 0.2 V. The resulting spectra are reported as the relative change in reflectivity, and calculated as follows

$$\frac{\Delta R}{R}(E_s) = \frac{R(E_s) - R(E_R)}{R(E_R)}$$

For each single-beam spectrum, 200 interferograms were added to increase the signal-to-noise ratio at a spectral resolution of 8 cm^{-1}.

2.5. MEA fabrication and single-cell tests

Commercial Nafion 115 membrane was used as the proton exchange membranes, and the pre-treatment process was accomplished by boiling in a 3 wt% H_2O_2 and 1 M H_2SO_4 solution for 1 h at 80 °C to remove impurities, then preserved in water for use. Membrane electrode assemblies (MEAs) with an active cell area of 1.14 cm^2 were activated in 3 M methanol solution and measured in a DMFCs testing setup. Four different anode catalysts were investigated in this study: PtRu/PC–H, PtRu/PC-L, commercial PtRu/C (40 wt% Pt and 20 wt% Ru, Johnson Matthey) and commercial Pt/C (60 wt% Pt, Johnson Matthey). The cathodic nanocatalyst was commercial 60 wt% Pt/C. The total metal loading both of anode and cathode nanocatalysts were a low content of 1 mg cm^{-2}. Those anodic catalyst inks were prepared by dispersing the nanocatalysts into the mixture of water, isopropanol and a 5 wt% Nafion solution, and then ultrasonically dispersed for 30 min. And the cathodic ink was prepared using the above way except for 15% PTFE added. All nanocatalysts inks were directly painted on a gas diffusion layer with a microporous layer. Hot-pressing was conducted at 120 °C and 1 M Pa for 100 s. Polarization curves were obtained using a Fuel Cell Test System (850e Multi range, Scribner Associate Co.) under the operating conditions of 75 °C with humidified O_2 flowing at a rate of 0.1 L min^{-1} and anode fuel was passed at 1.0 mL min^{-1}.

3. Results and discussion

3.1. XRD, EDX, TEM and XPS characterization of electrocatalysts

XRD studies were conducted to examine the crystal structures and the type of diffraction peaks, Fig. 1A presents the XRD patterns of PtRu/

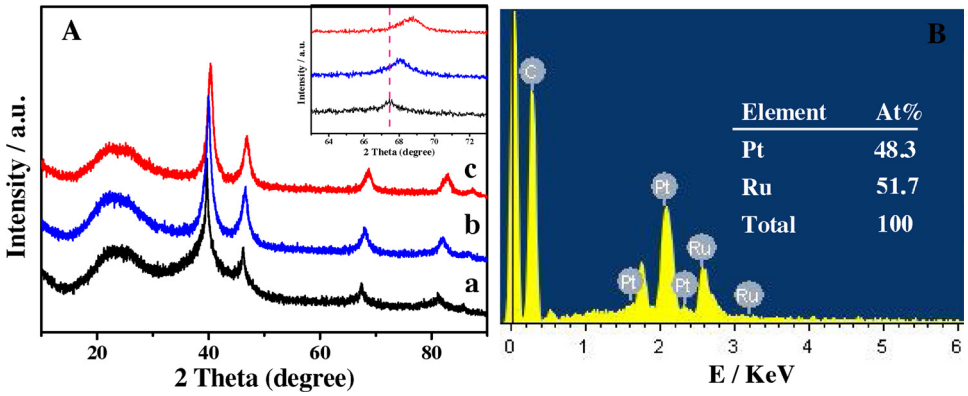

Fig. 1. (A) XRD patterns of Pt/PC (a), PtRu/PC-L (b) and PtRu/PC–H (c) samples. (B) The EDX of PtRu/PC–H nanocatalyst. The inset is the magnified picture of the partial region in A.

PC and Pt/PC nanocatalysts. The five dominant peaks at 2θ = 39.7°, 46.2°, 67.5°, 81.2° and 85.7° correspond to the (111), (200), (220), (311) and (222) planes of Pt face-centered cubic (fcc) structure in curve a, respectively (JCPDS card NO. 65-2868). As seen from the curve b and c, the PC support nanoparticles reveal the standard patterns of fcc Pt and without observation the diffraction peaks of hexagonal close-packed Ru or its oxides, which indicate no phase separation and bi-metallic PtRu nanoparticles are alloys. Visibly, the diffraction peaks of PtRu/PC possess higher 2θ values than that of Pt/PC nanocatalyst (inset of Fig. 1A), because of the incorporation of smaller Ru atoms into the Pt lattice and the formation of PtRu alloys nanostructure. PtRu/PC–H and PtRu/PC-L have positive shift 2θ values about 1.2 and 0.6, respectively, implying the appearance of compressive strains on the crystal lattice of PtRu alloy and the annealed nanoalloy at 700 °C with higher alloying degree [3,22]. Lattice contraction and the reduction of Pt–Pt distance possible cause the favoring adsorption and/or desorption for reactants and enhancing their catalytic performance. In terms of the Pt(220) peak and the Scherrer formula, the average crystal size of PtRu-H, PtRu-L and Pt/PC nanoparticles in three nanocatalysts were calculated to be about 2.92, 2.71 and 2.25 nm, respectively. Beyond that, EDX analysis confirms the presence of Pt and Ru in PtRu/PC–H nanocatalyst and the atomic ratio of Pt/Ru is 48.3/51.7 (Fig. 1B), which is in accordance with the ICP-OES measurement and the corresponding value in the precursor solutions.

More information about the morphology and structure of samples can be obtained by the TEM measurements. Fig. 2 shows the representative TEM images of PtRu/PC and Pt/PC nanocatalysts. As presented in Fig. 2A, B and C, small nanoparticles are very uniformly distribute on the PC support. The statistic histograms for more than 200 nanoparticles measured in the TEM random regions suggest that the PtRu/PC–H, PtRu/PC-L and Pt/PC nanoparticles have an average size of 2.82, 2.69 and 2.20 nm and with a narrow size distribution (Fig. 2D, E and F), such particles size are very close to those from XRD results. It is interesting to note that the small, uniform and high alloying degree PtRu/PC–H nanoparticles have been achieved under hydrogen at 700 °C. Small size nanoparticles often occur diffusion and agglomeration phenomenon under high-temperature anneal, such as XC-72 support PtRu nanoparticles (Fig. S2), however, the PC with porous structure and great surface area (BET = 1066 $m^2 g^{-1}$) is of great importance to adsorb metal precursor and afford good tolerance to the undesired agglomeration [38]. Moreover, the porous structure and higher BET surface area of PC is favorable for electron transfer and mass transfer in electrocatalytic reaction, so that enhancing the catalytic performance [35]. The highly magnified images of an individual PtRu/PC–H, PtRu/PC-L and Pt/PC nanoparticles display its obvious lattice fringe, and interplanar distance is 0.22, 0.22 and 0.23 nm, respectively, ascribed to the {111} plane of a typical Pt fcc structure. The high dispersive PtRu/PC–H alloy nanoparticles can provide much higher surface area and atom utility, which is very important for MOR electrocatalysts.

To further examine the electronic structures and chemical valence state of as-prepared nanocatalysts, we employed XPS measurements to investigate the samples. The XPS wide survey spectrums of PtRu/PC–H, PtRu/PC−L, Pt/PC and Ru/PC were shown in Fig. 3. Compared with the Pt/PC and Ru/PC (curve d and c), the coexistence of Pt and Ru signals in the spectrum of PtRu/PC nanocatalysts (curve a and b), which is in agreement with the EDX, also indicating that the PtRu/PC nanocatalysts are successfully prepared. Fig. 4A, B and C show the Pt 4f high-resolution spectra of Pt/PC, PtRu/PC−L and PtRu/PC–H, which could be divided into two pairs of doublets. As depicted by Pt/PC (Fig. 4A), two pairs of fitting peaks represent two different valence states of Pt on nanocatalysts surface. Two strong peaks at 71.0 eV (Pt $4f_{7/2}$) and 74.5 eV (Pt $4f_{5/2}$) were corresponding to the metallic Pt, and the weak peaks located at 71.8 eV (Pt $4f_{7/2}$) and 75.7 eV (Pt $4f_{5/2}$) were attributed to the Pt (II) species, such as PtO or $Pt(OH)_2$. For the PtRu/PC−L catalyst (Fig. 4B), the similar XPS signals of metallic Pt (71.4 eV for Pt $4f_{7/2}$, 74.9 eV for Pt $4f_{5/2}$) and Pt (II) species (72.0 eV for Pt $4f_{7/2}$, 76.3 eV for Pt $4f_{5/2}$) are also observed. In the PtRu/PC–H nanocatalyst (Fig. 4C), two stronger peaks locate at 71.6 and 75.1 eV, the weaker doublet locates 72.5 and 76.2 eV, which could be assigned to metallic and oxidized Pt, respectively. According to the measured relative peak areas, the percentage of metallic Pt for PtRu/PC–H, PtRu/PC−L and Pt/PC samples is 64.1%, 49.8% and 59.9%, respectively. Metallic Pt is the most significant active sites for MOR, PtRu/PC–H with more zero valences possibly easily promote the C–H cleavage reaction at low potentials [7]. Additionally, we can observe that the peak position of PtRu/PC–H and PtRu/PC−L are shifted positively (0.5 and 0.3 eV) than that for the Pt/PC. The positive binging energy of Pt 4f is attributed to the difference in the work function of Pt and PtRu, and the rehybridization of both d-band and sp-band of Pt atoms in the PtRu alloy. Positive shifts of the binding energy in Pt atoms indicates the downshift of the d-band center and decreases the electron back-donation from Pt 5d orbital to the 2p* orbital of CO, thus causes the weakening of CO-Pt bonding [39]. The XPS analysis further confirms the presence of strong electronic transfer interaction between Pt and alloyed Ru, which Ru could modify the electronic structure of Pt. From the Ru 3p high-resolution XPS spectrum (Fig. 4D) of Ru/PC, we can observe two pairs of deconvoluted peaks, which are resolved into two different valence states of Ru element. The peaks at 462.3 eV and 484.4 eV are attributed to the metallic Ru, and the peaks at 464.1 eV and 487.8 eV are assigned to the RuO_2 species [40]. As can be seen from Fig. 4E, the Ru 3p of PtRu/PC−L also appears two pairs of deconvoluted peaks. Two peaks at 462.2 eV and 485.1 eV are assigned to the metallic Ru, and the peaks at 464.5 eV and 488.0 eV are assigned to the Ru(II) species. For the PtRu/PC–H (Fig. 4F), the similar deconvoluted peaks of metallic Ru (461.9 eV for Ru $3p_{3/2}$ and 483.8 eV for Ru $3p_{1/2}$) and Ru (II) species (464.9 eV for Ru $3p_{3/2}$ and 486.8 eV or Ru $3p_{1/2}$) are observed. By calculating, we also could obtain the percentage of metallic Ru for PtRu/PC–H, PtRu/PC−L, Ru/PC is about 35.7%, 40.8% and 67.0%, respectively, suggesting that most Ru on the catalytic surface of PtRu/PC–H exist in the oxide form. What's more, the binding energy of metallic Ru in the PtRu/PC–H and PtRu/PC−L have a negative shift (0.5 and 0.3 eV) compared with the corresponding value of Ru/PC. By alloying Pt with Ru, possible electronic and/or strain effects could cause the downshifts of d-band center of Pt and enhance MOR catalytic performance [3]. This is consistent with XRD; smaller size Ru atoms compress the lattice of Pt, which could lower their d-band centers. The positive shifts phenomenon of Pt 4f gives Pt-based alloy more 5d orbital vacancies and a less filled 5d orbital, which reduces the bond energy of $Pt-CO_{ads}$ [1,41]. Moreover, Wakisaka et al. [42] researched the electronic structures of Pt, PtCo and PtRu using XPS combined with an electrochemical cell and exposed the Pt-based alloys to cause the positive shift of Pt $4f_{7/2}$ and weaken the CO adsorption energy. Therefore, because of the stronger charge transfer interaction between Pt and Ru atoms, the surface adsorption ability of small adsorbates (like CO_{ads}) for PtRu/PC–H would be weakened and the catalytic performance for MOR will be improved.

3.2. Electrochemical performance of electrocatalysts

Fig. 5A shows the cyclic voltammetry curves of PtRu/PC–H, PtRu/PC−L and Pt/PC nanocatalysts. The mass activity in all electrochemical tests was normalized by per milligram of Pt loading. As seen from the curves, three nanocatalysts exhibit typical CV characteristics of Pt-based samples with hydrogen adsorption/desorption regions (below 0.1 V) and Pt oxidation/reduction peaks at high potentials. Among three samples, the double-layer capacitances decrease in the order of PtRu/PC−L > PtRu/PC–H > Pt/PC, the broadest feature of double layer charging current confirms the PtRu/PC−L surface enriched with Ru atoms [43]. Taking the work of Wu's group for example [44,45], they found the double-layer capacitive current is proportional to the amount of Ru atoms on PtRu and PdRu nanocatalysts surface. Compared with PtRu/PC−L nanocatalyst, the decrease in double-layer capacitive current for PtRu/PC–H sample reveals, annealed at high

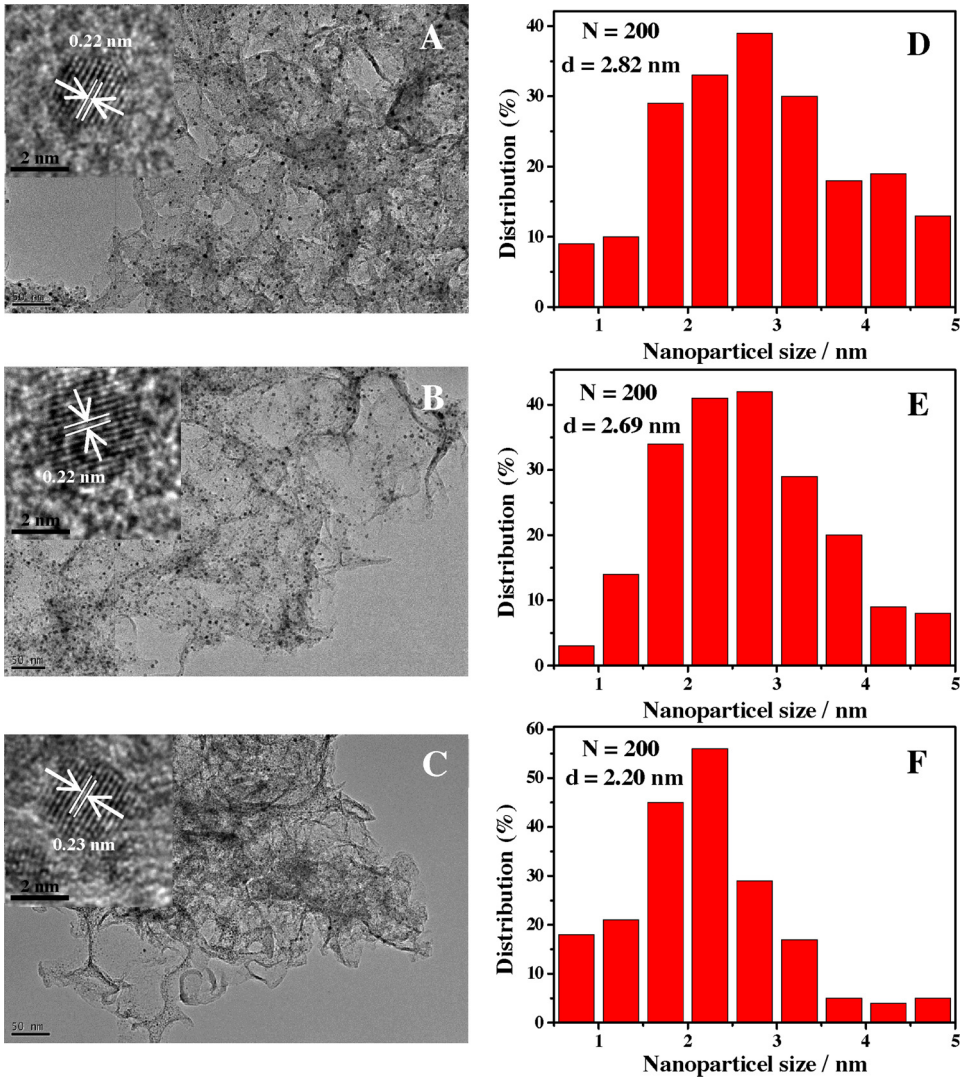

Fig. 2. TEM images and the corresponding size distribution histograms of PtRu/PC–H (A and D), PtRu/PC-L (B and E) and Pt/PC (C and F) samples. The inset is the HRTEM image of PtRu/PC–H, PtRu/PC-L and Pt/PC in A, B and C, respectively.

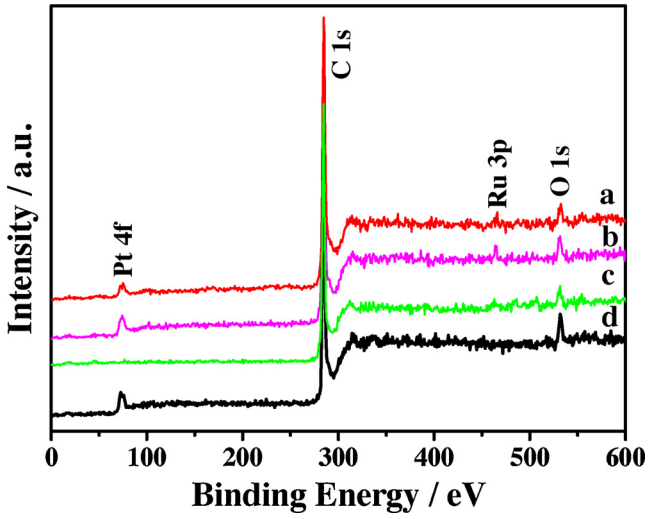

Fig. 3. XPS survey spectra of PtRu/PC–H (a), PtRu/PC-L (b), Ru/PC (c) and Pt/PC (d) samples.

temperatures, PtRu nanoalloys undergo phase segregation in which the Pt migrates to the surface, forming a Pt-increased alloy nanostructure, since the adsorption enthalpy of H on Pt is higher than that on Ru [46,47]. As the work of Wang et al. for example [48], the surface segregation energy of Pt@Ru is a negative value, suggesting there would be a much stronger driving force for Pt atoms to the surface of nanoparticles. Moreover, it can be seen that the reduction peaks of surface Pt oxides for PtRu/PC are negatively shifted compared to the Pt/PC nanocatalyst, indicating that the PtRu/PC possesses more strong hydroxyl adsorption ability at more negative potentials [49]. The ECSA is an important parameter for electrocatalysts, the values of PtRu/PC–H, PtRu/PC−L and Pt/PC are 38.0, 23.9 and 82.9 $m^2 g_{Pt}^{-1}$. The higher ECSA of Pt/PC than PtRu/PC results from the high Pt content and most active sites on the surface. The Pt/PC possess higher ECSA compared with literatures reported commercial Pt/C (69.8 $m^2 g_{Pt}^{-1}$) [50], Pt/P-MCNTs (78.9 $m^2 g_{Pt}^{-1}$) [51] and MWNTs/Pdop-Pt (60.8 $m^2 g_{Pt}^{-1}$) [52], should be originated from smaller size of Pt nanoparticles, much better dispersion of nanoparticles on PC and the unique porous structure of PC.

On account of the reduction potential of H_2PtCl_6 is higher than that of $RuCl_3$, Pt nuclei could be preferentially formed over Ru in H_2 gas. Whereafter, Pt nucleis were served as catalytic sites to further reduce the Ru precursor via autocatalytic process, and both Pt and Ru atoms

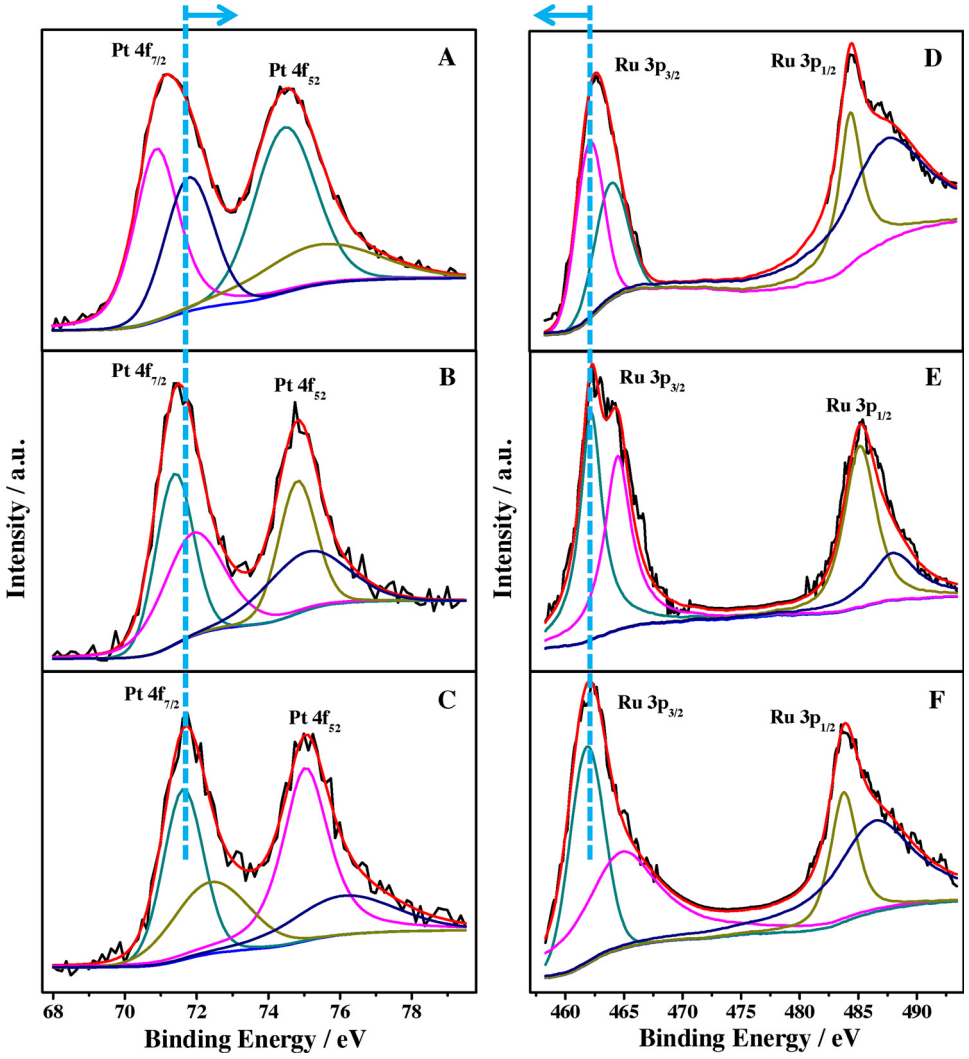

Fig. 4. Pt 4f XPS spectra for Pt/PC (A), PtRu/PC-L (B), PtRu/PC–H (C) nanocatalysts; Ru 3p XPS spectra for Ru/PC (D), PtRu/PC-L (E), PtRu/PC–H (F) nanocatalysts.

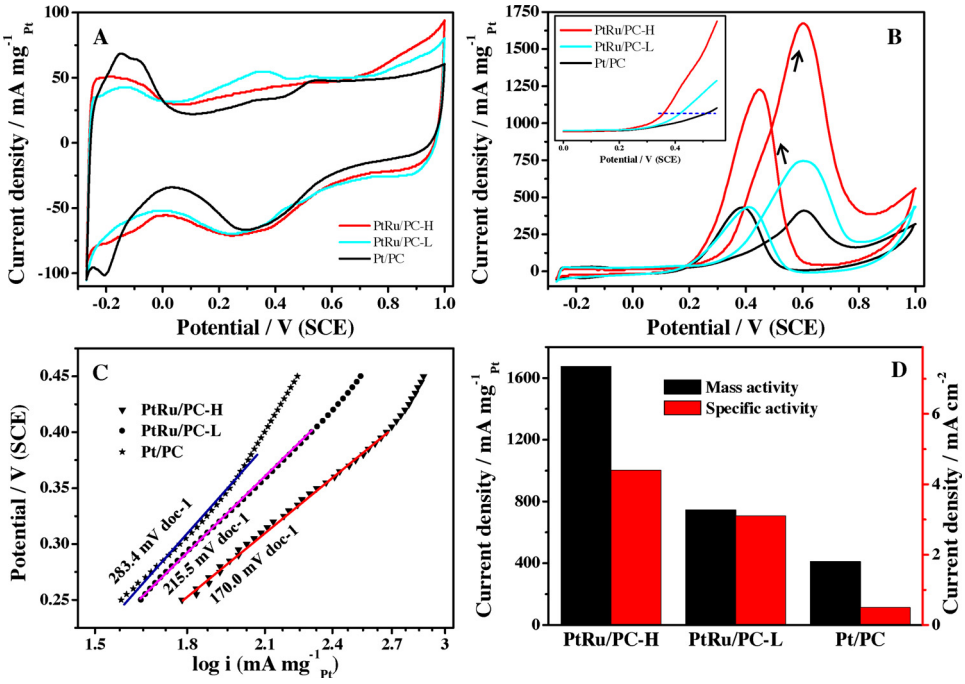

Fig. 5. (A) Cyclic voltammograms in 0.1 M $HClO_4$ solution (B) MOR in 0.5 M CH_3OH + 0.1 M $HClO_4$ solution for PtRu/PC–H, PtRu/PC-L, Pt/PC nanocatalysts at a scan rate of 50 mV s^{-1} (the inset is the magnified CV in the potential range of 0 ~ 0.55 V). (C) The Tafel curves for methanol electrooxidation on different catalysts in 0.1 M $HClO_4$ solutions containing 0.5 M CH_3OH. (D) Comparisons of the mass and specific activities of three catalysts.

deposit on the surfaces of Pt nuclei followed by growth formation of small alloyed PtRu nanoparticles [19,53]. Inspired by the control of their attractive nanostructure in H_2, the MOR activities of as-prepared PtRu nanocatalysts were tested and benchmarked relative to the Pt/PC nanocatalyst. Fig. 5B displays the electrocatalytic properties of PtRu/PC–H, PtRu/PC—L and Pt/PC catalysts for methanol oxidation. Three curves display two well-defined irreversible oxidation peaks during MOR, in which the forward peak is due to the direct oxidation of methanol molecules and intermediates at about 0.60 V, and another anodic peak (0.45 V) in the backward scan might be attributed to the oxidation of re-adsorbed CH_3OH associated with the reactivation of oxidized Pt after the CO_{ads} oxidation at high potential. MOR electrocatalytic performance of different nanocatalysts can be compared by the oxidation potential and the peak current density for methanol oxidation. The potential of MOR on PtRu/PC–H is shifted to more negative than those on PtRu/PC—L and Pt/PC. Meanwhile, in the forward direction scan, PtRu/PC–H exhibits a highest peak current density (1674.2 mA mg_{Pt}^{-1}), that is about 2.25 and 4.08 times high than that of PtRu/PC—L (744.7 mA mg_{Pt}^{-1}) and Pt/PC (410.0 mA mg_{Pt}^{-1}) nanocatalysts, respectively. The mass activity normalized by total metal loading also is presented in Fig. S3, PtRu/PC–H also has the best MOR activity (1080.1 mA mg_{Pt+Ru}^{-1}), that is about 2.10 and 2.63 times than that of PtRu/PC—L (513.9 mA mg_{Pt+Ru}^{-1}) and Pt/PC (410.0 mA mg_{Pt}^{-1}) nanocatalysts, respectively. Interestingly, the methanol oxidation potentials of PtRu/PC–H at any positions are significantly lower than other both catalysts. As shown by the dotted line in the inset of Fig. 5B, PtRu/PC–H oxidation potential negatively shifted by 61 and 152 mV compared to PtRu/PC—L and Pt/PC nanocatalysts at the current density of 250 mA mg_{Pt}^{-1}. Tafel slope is a significant kinetic parameter in various electrocatalytic reactions. Tafel slope was calculated on the PtRu/PC–H, PtRu/PC—L and Pt/PC nanocatalysts shown in Fig. 5C, the value is 170.0, 215.5 and 283.4 mV dec^{-1}, respectively. PtRu/PC—H shows the lowest Tafel slope among these nanocatalysts, indicating the faster dehydrogenation on CH_3OH molecule and the superior kinetics reaction process. The Tafel slope is similar to the literature reported slope [54]. Therefore, PtRu/PC–H nanoalloy could cleave the C–H bond for CH_3OH at lower potentials. These results strongly reveal that the methanol oxidation more easily occurs on the surface of PtRu/PC–H nanocatalyst than others. The specific activity of PtRu/PC–H (4.41 mA cm^{-2}) is 1.42 and 8.80 times higher than those of PtRu/PC—L (3.11 mA cm^{-2}) and Pt/PC (0.50 mA cm^{-2}) nanocatalysts, respectively (Fig. 5D). It's worth noting that the catalytic performance of PtRu/PC–H is higher than that the previously reported PtRu/CuNWs (450 mA mg_{PtRu}^{-1}, 1 M methanol) [12], PtRu nanodendrites (1080 mA mg_{Pt}^{-1}) [19], core-shell Fe@(PtRu) (819.1 mA mg_{Pt}^{-1}) [55], PtRu/G_{75}-$(CN)_{25}$ (910.0 mA mg_{Pt}^{-1}) [56], and PtRu/NCNHs (850 mA mg_{PtRu}^{-1}, 1 M methanol) [57]. The enhanced performance of PtRu/PC–H nanocatalyst is considered to relate to the bifunctional effects, strain effects and ligand effects.

To compare the CO tolerance ability in electrocatalytic reaction, the CO stripping experiments were executed. Fig. 6 shows the CO stripping voltammograms and the subsequent CV curves of three catalysts in 0.1 M $HClO_4$ solution. We can hardly observe the adsorption and desorption signals of hydrogen for all the catalysts in the first scan, indicating that the surface active sites of these catalysts are completely poisoned by the CO_{ads} species. In the subsequent CV curves, the CO oxidation peaks disappear and the corresponding hydrogen adsorption and desorption peaks renew, demonstrating the complete oxidation removal of CO_{ads} species. Most importantly, the onset potential of CO_{ads} oxidation on the PtRu/PC–H (Fig. 6A) is 0.16 V, about 80 and 280 mV more negative than that on the PtRu/PC—L (0.24 V, Fig. 6B) and Pt/PC (0.44 V, Fig. 6C) nanocatalysts, respectively. Compared with the Pt/PC and PtRu/PC—L nanocatalysts, it can be obtained the CO tolerance ability of PtRu/PC–H was significantly enhanced by alloying with Ru and high-temperature annealing. Moreover, the easier of CO oxidation on PtRu/PC than that on Pt/PC nanocatalyst reflects the effectiveness of electron coupling between the Pt and Ru. The electron effect and strain

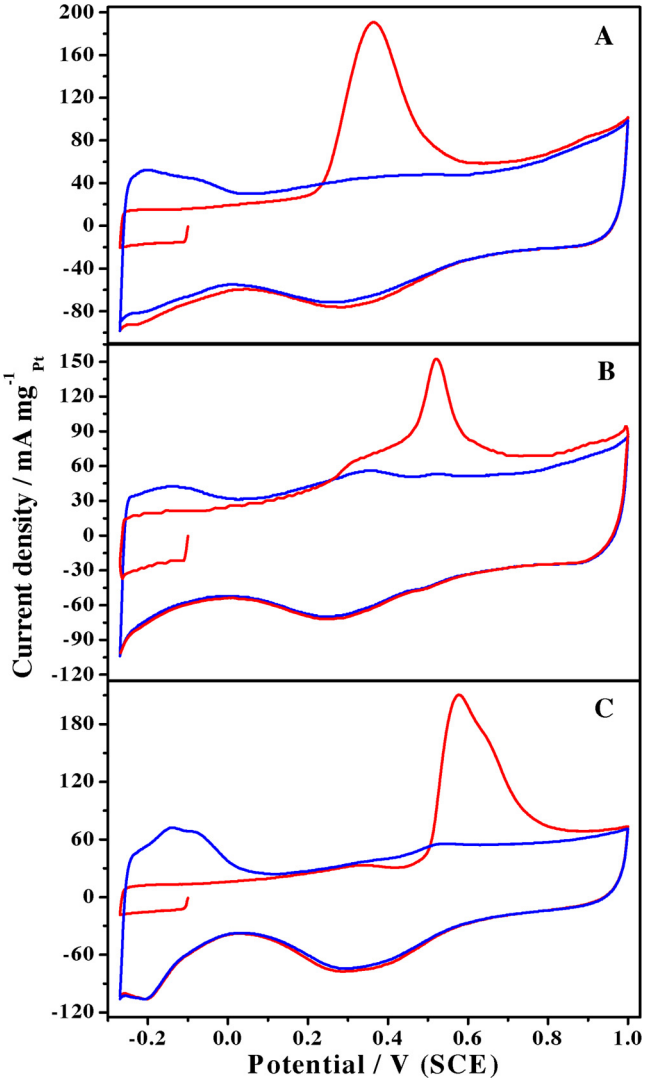

Fig. 6. CO stripping voltammograms of PtRu/PC–H (A), PtRu/PC-L (B), Pt/PC (C) nanocatalysts in 0.1 M $HClO_4$ solution at a scan rate of 50 mV s^{-1}.

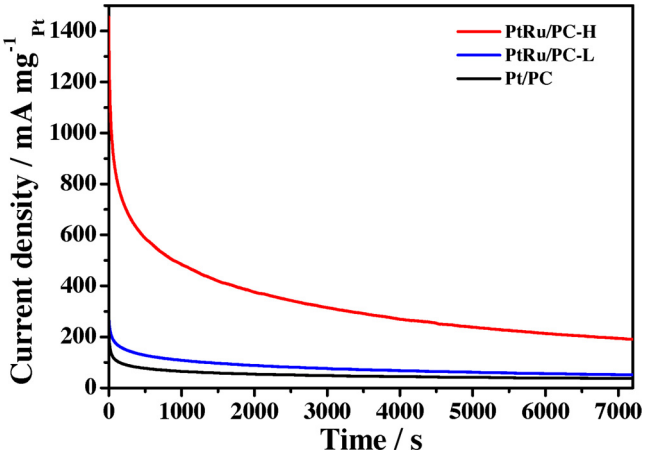

Fig. 7. Current-time curves of methanol oxidation on PtRu/PC–H, PtRu/PC-L and Pt/PC nanocatalysts in 0.5 M CH_3OH + 0.1 M $HClO_4$ solution at a potential of 0.5 V.

effect resulted from the lattice mismatch of Pt and Ru atoms, decreases the binding energies of reaction intermediates and d-band center of Pt near the Fermi level, thus provides high CO-tolerance [58].

Chronoamperometry (CA) curves were recorded in 0.5 M CH_3OH + 0.1 M $HClO_4$ solution under a constant potential of 0.5 V, as shown in Fig. 7. The high initial current density was caused by double-layer charging and abundant active sites for methanol activation, and then the current density dropped quickly within the first dozens of seconds due to the adsorption of CO-like by-products from the MOR on the catalytic surface. After the 7200 s tests, the PtRu/PC–H still presents the highest limiting current density (195.4 mA mg_{Pt}^{-1}) compared with the PtRu/PC-L (51.0 mA mg_{Pt}^{-1}) and Pt/PC (36.7 mA mg_{Pt}^{-1}) nanocatalysts, further confirming that the PtRu/PC–H nanocatalyst possesses the best electrocatalytic activity and long-term electrochemical durability for MOR. We as-synthesized PtRu/PC–H nanoparticles possess a large proportion of surface area to volume, higher alloying degree, stronger electronic interaction between Pt and Ru atoms, clear surface and more available active sites, so that it could dramatically enhanced electrocatalytic performance for MOR.

3.3. In situ FTIR spectroscopy studies for MOR

Despite methanol is a simple small organic molecule, the exact mechanism is complicated, involving a lot of intermediate species, products, and byproducts. [59] In-situ FTIR spectra technique is sensitive to identify intermediates and products at the electrocatalytic reaction process [60]. Herein, the possible reason for annealing facilitates the arresting enhanced performance for MOR is also verified by in-situ FTIR spectra at a molecular level. FTIR spectra of three samples recorded in 0.5 M CH_3OH + 0.1 M $HClO_4$ are exhibited in Fig. 8A − C, respectively. The negative band at about 2050 cm^{-1} was assigned to linearly bonded CO_{ads} (CO_L) species at Pt sites. Compared with Pt/PC sample, PtRu/PC nanocatalysts had a more negative adsorbed − CO potential, implied that dissociative adsorption of methanol to form CO_{ads} easily occurs at − 0.15 V for the PtRu/PC nanocatalysts. Moreover, the intensity of CO_{ads} for Pt/PC is incremental with test procedure, indicated the nanocatalyst surface is heavily poisoned by CO within the potential range [32]. The effect of Ru alloyed Pt is most obvious from the appearance of a CO_2 signal (2345 cm^{-1}) at − 150 mV for PtRu/PC–H (Fig. 8A), 150 and 200 mV lower than the onset potential of the PtRu/PC−L (0 mV) and Pt/PC (50 mV), respectively. This

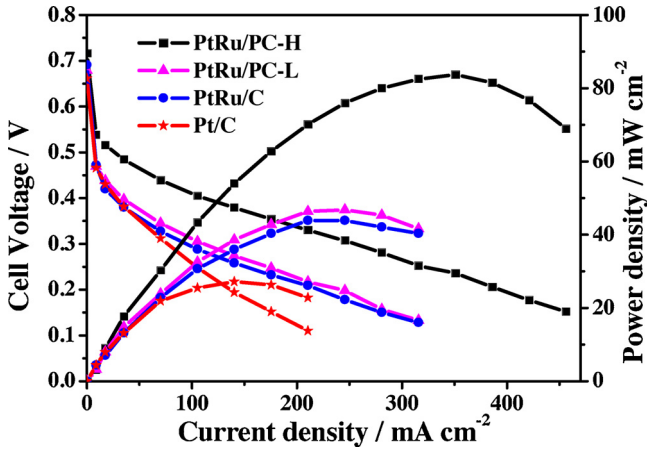

Fig. 9. Steady-state polarization and power density curves for fuel cells employing PtRu/PC–H, PtRu/PC-L, commercial PtRu/C and commercial Pt/C as anode catalysts.

is in strong accord with the electrochemical measurement results of Fig. 5B and 5C, which showed a decrease in onset oxidation potential and easy cleavage C–H bond of CH_3OH for PtRu/PC–H nanocatalyst.

3.4. Single-cell tests

For the practical application, the single-cell acidic DMFCs based on as-prepared PtRu anode catalysts were assembled for potential performance assessment. For comparison, the commercial Pt/C and PtRu/C anode catalysts were used. Fig. 9 shows the steady-stead polarization and power density curves of four samples under 75 °C testing condition. Obviously, the fuel cell with PtRu/PC–H anode catalyst exhibits the highest current density than all other fuel cells at the same potential. As a result, this fuel cell has the highest power density as well, with a maximum power density of 83.7 mW cm^{-2}, which is about 1.8, 1.9 and 3.1 times than those of PtRu/PC-L, commercial PtRu/C and Pt/C nanocatalysts, respectively. The power density of PtRu/PC–H (1 mg cm^{-2}) is also higher than those of the PtRu nanocatalysts with 2 mg

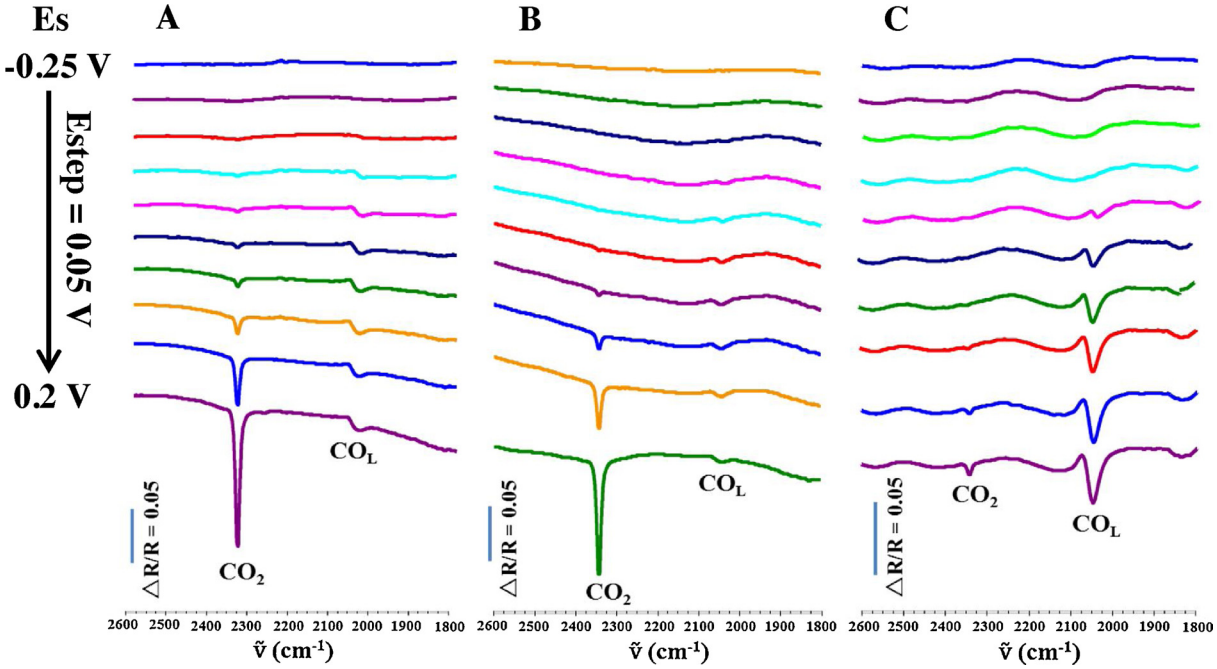

Fig. 8. In situ FTIR spectra for methanol electrooxidation on PtRu/PC–H (A), PtRu/PC-L (B), Pt/PC (C) catalyst in 0.5 M CH_3OH + 0.1 M $HClO_4$ solution. The reference spectra were acquired at − 0.27 V.

cm^{-2} metal loading, such as PtRu/C/Nafion/PVA (44 mW cm^{-2}), PtRu/Porous MPL and CL (43.7 mW cm^{-2}), PtRu/C + 20% IrO_2 (23 mW cm^{-2}) and PtRuMo/CNTs (61.3 mW cm^{-2}) [61–64]. Meanwhile, the discharging voltages at the loading current density of 200 mA cm^{-2} for PtRu/PC–H, PtRu/PC-L, PtRu/C and Pt/C are 0.12, 0.22, 0.23 and 0.34 V, respectively. It can be seen that PtRu/PC–H is a promising anode nanocatalyst for DMFCs.

4. Conclusions

In summary, uniform and small size PtRu nanoparticles supported on the PC surface have been successfully synthesized through simple hydrogen co-reduction strategy at 300 °C followed by high-temperature treatment at 700 °C and used as high-efficient MOR nanocatalyst. Thanks to the synergistic effects of several factors such as the abundant accessible active sites, high alloying degree, strong electronic interaction between Pt and Ru atoms, and special porous structure of PC, the as-prepared PtRu/PC–H exhibits enhanced electrocatalytic activity, durability and CO tolerance ability compared with PtRu/PC—L and Pt/PC nanocatalysts. In addition, we obtain the important information from in situ FTIR spectroscopy that PtRu/PC–H could easily cleave C–H bond and oxidate CO_{ad} at lower potential. A direct methanol fuel cell employing the optimized PtRu/PC–H anode catalyst has a maximum power density that is 3.1 times than that of analogous fuel cells employing commercial Pt/C catalysts. The efficient approach is a highly promising and alternative route for the design and synthesis of high-performance electrocatalysts for fuel cells applications.

Declaration of Competing Interest

The authors declare no competing financial interest.

Acknowledgments

This study was supported by grants from the National Key Research and Development Program of China (2017YFA0206500), and the National Natural Science Foundation of China (21773198, U1705253 and 21621091).

References

[1] Y. Zhao, J. Liu, C. Liu, F. Wang, Y. Song, ACS Catal. 6 (2016) 4127–4134.
[2] Z. Cui, H. Chen, M. Zhao, D. Marshall, Y. Yu, H. Abruna, F.J. DiSalvo, J. Am. Chem. Soc. 136 (2014) 10206–10209.
[3] P. Wang, S. Yin, Y. Wen, Z. Tian, N. Wang, J. Key, S. Wang, P.K. Shen, ACS Appl. Mater. Interfaces 9 (2017) 9584–9591.
[4] W. Gong, Z. Jiang, R. Wu, Y. Liu, L. Huang, N. Hu, P. Tsiakaras, P.K. Shen, Appl. Catal. B 246 (2019) 277–283.
[5] Y. Wang, M. Zheng, H. Sun, X. Zhang, C. Luan, Y. Li, L. Zhao, H. Zhao, X. Dai, J.Y. Ye, H. Wang, S.G. Sun, Appl. Catal. B 253 (2019) 11–20.
[6] Z. Dasdelen, Y. Yildiz, S. Eris, F. Sen, Appl. Catal. B 219 (2017) 511–516.
[7] X. Du, S. Luo, H. Du, M. Tang, X. Huang, P.K. Shen, J. Mater. Chem. A Mater. Energy Sustain. 4 (2016) 1579–1585.
[8] E. Lee, S. Kim, J.H. Jang, H.U. Park, M.A. Matin, Y.T. Kim, Y.U. Kwon, J. Power Sources 294 (2015) 75–81.
[9] L. Huang, J. Zou, J.Y. Ye, Z.Y. Zhou, Z. Lin, X. Kang, P.K. Jain, S. Chen, Angew. Chem. Int. Ed. 58 (2019) 1–6.
[10] Q. Zhang, F. Yue, L. Xu, C. Yao, R.D. Priestley, S. Hou, Appl. Catal. B 257 (2019) 117886–117893.
[11] C. Bock, C. Paquet, M. Couillard, G.A. Botton, B.R. MacDougall, J. Am. Chem. Soc. 126 (2004) 8028–8037.
[12] J. Zheng, D.A. Cullen, R.V. Forest, J.A. Wittkopf, Z. Zhuang, W. Sheng, J.G. Chen, Y. Yan, ACS Catal. 5 (2015) 1468–1474.
[13] J. Wang, Z. Wang, S. Li, R. Wang, Y. Song, Nanoscale 9 (2017) 4066–4075.
[14] Z. Zhang, Z. Luo, B. Chen, C. Wei, J. Zhao, J. Chen, X. Zhang, Z. Lai, Z. Fan, C. Tan, M. Zhao, Q. Lu, B. Li, Y. Zong, C. Yan, G. Wang, Z.J. Xu, H. Zhang, Adv. Mater. 28 (2016) 8712–8717.
[15] S. Lu, K. Eid, M. Lin, L. Wang, H. Wang, H. Gu, J. Mater. Chem. A Mater. Energy Sustain. 4 (2016) 10508–10513.
[16] Z. Qi, C. Xiao, C. Liu, T.W. Goh, L. Zhou, R. Maligal-Ganesh, Y. Pei, X. Li, L.A. Curtiss, W. Huang, J. Am. Chem. Soc. 139 (2017) 4762–4768.
[17] L. Huang, Y. Han, X. Zhang, Y. Fang, S. Dong, Nanoscale 9 (2017) 201–207.
[18] Q. Chen, Y. Yang, Z. Cao, Q. Kuang, G. Du, Y. Jiang, Z. Xie, L. Zheng, Angew. Chem. Int. Ed. 55 (2016) 1–6.
[19] S. Lu, K. Eid, D. Ge, J. Guo, L. Wang, H. Wang, H. Gu, Nanoscale 9 (2017) 1033–1039.
[20] J. Zhu, Y. Yang, L. Chen, W. Xiao, H. Liu, H.D. Abruna, D. Wang, Chem. Mater. 30 (2018) 5987–5995.
[21] W.Y. Zhao, B. Ni, Q. Yuan, P.L. He, Y. Gong, L. Gu, X. Wang, Adv. Energy Mater. 7 (2017) 1601593–1601600.
[22] L. Feng, K. Li, J. Chang, C. Liu, W. Xing, Nano Energy 15 (2015) 462–469.
[23] T. Takeguchi, T. Yamanaka, K. Asakura, E.N. Muhamad, K. Uosaki, W. Ueda, J. Am. Chem. Soc. 134 (2012) 14508–14512.
[24] M. Xiao, L. Feng, J. Zhu, C. Liu, W. Xing, Nanoscale 7 (2015) 9467–9471.
[25] Z. Lin, W. Chen, Y. Jiang, T. Bian, H. Zhang, J. Wu, Y. Wang, D. Yang, Nanoscale 8 (2016) 12812–12818.
[26] L. Huang, X. Zhang, Q. Wang, Y. Han, Y. Fang, S. Dong, J. Am. Chem. Soc. 140 (2018) 1142–1147.
[27] S. Alayoglu, P. Zavalij, B. Eichhorn, Q. Wang, A.I. Frenkel, P. Chupas, ACS Nano 3 (2009) 3127–3137.
[28] M. Huang, C. Wu, L. Guan, J. Power Sources 306 (2016) 489–494.
[29] L. Zou, J. Guo, J. Liu, Z. Zou, D.L. Akins, H. Yang, J. Power Sources 248 (2014) 356–362.
[30] Z. Bo, D. Hu, J. Kong, J. Yan, K. Cen, J. Power Sources 273 (2015) 530–537.
[31] Q. Feng, S. Zhao, D. He, S. Tian, L. Gu, X. Wen, C. Chen, Q. Peng, D. Wang, Y. Li, J. Am. Chem. Soc. 140 (2018) 2773–2776.
[32] D.J. Chen, Y.J. Tong, Angew. Chem. Int. Ed. 54 (2015) 9394–9398.
[33] X. Lu, Z. Deng, C. Guo, W. Wang, S. Wei, S.P. Ng, X. Chen, N. Ding, W. Guo, C.M.L. Wu, ACS Appl. Mater. Interfaces 8 (2016) 12194–12204.
[34] H.X. Liu, N. Tian, M.P. Brandon, Z.Y. Zhou, J.L. Lin, C. Hardacre, W.F. Lin, S.G. Sun, ACS Catal. 2 (2012) 708–715.
[35] G.L. Xu, Y.F. Xu, J.C. Fang, X.X. Peng, F. Fu, L. Huang, J.T. Li, S.G. Sun, ACS Appl. Mater. Interfaces 5 (2013) 10782–10793.
[36] B.W. Zhang, Z.C. Zhang, H.G. Liao, Y. Gong, L. Gu, X.M. Qu, L.X. You, S. Liu, L. Huang, X.C. Tian, R. Huang, F.C. Zhu, T. Liu, Y.X. Jiang, Z.Y. Zhou, S.G. Sun, Nano Energy 19 (2016) 198–209.
[37] J.Y. Ye, Y.X. Jiang, T. Sheng, S.G. Sun, Nano Energy 29 (2016) 414–427.
[38] Z.C. Zhang, X.C. Tian, B.W. Zhang, L. Huang, F.C. Zhu, X.M. Qu, L. Liu, S. Liu, Y.X. Jiang, S.G. Sun, Nano Energy 34 (2017) 224–232.
[39] H. Igarashi, T. Fujino, Y. Zhu, H. Uchida, M. Watanabe, Phys. Chem. Chem. Phys. 3 (2001) 306–314.
[40] G.H. An, E.H. Lee, H.J. Ah, Phys. Chem. Chem. Phys. 18 (2016) 14859–14866.
[41] G. Zhang, Z. Yang, W. Zhang, Y. Wang, J. Mater. Chem. A Mater. Energy Sustain. 9 (2016) 3316–3323.
[42] M. Wakisaka, S. Mitsui, Y. Hirose, K. Kawashima, H. Uchida, M. Watanabe, J. Phys. Chem. B 110 (2006) 23489–23496.
[43] T. Huang, D. Zhang, L. Xue, W.B. Cai, A. Yu, J. Power Sources 192 (2009) 285–290.
[44] Y. Sun, Y.C. Hsieh, L.C. Chang, P.W. Wu, J.F. Lee, J. Power Sources 277 (2015) 116–123.
[45] C.W. Kuo, I.T. Lu, L.C. Chang, Y.C. Hsieh, Y.C. Tseng, P.W. Wu, J.F. Lee, J. Power Sources 240 (2013) 122–130.
[46] D. Wang, H.L. Xin, Y. Yu, H. Wang, E. Rus, D.A. Muller, H.D. Abruna, J. Am. Chem. Soc. 132 (2010) 17664–17666.
[47] N.M. Popova, L.V. Babenkova, React. Kinet. Catal. Lett. 11 (1979) 187–192.
[48] L.L. Wang, D.D. Johnson, J. Am. Chem. Soc. 131 (2009) 14023–14029.
[49] R. Li, Z. Wei, T. Huang, A. Yu, Electrochim. Acta 56 (2011) 6860–6865.
[50] J.J. Fan, Y.J. Fan, R.X. Wang, S. Xiang, H.G. Tang, S.G. Sun, J. Mater. Chem. A Mater. Energy Sustain. 5 (2017) 19467–19475.
[51] Z. Liu, Q. Shi, F. Peng, H. Wang, R. Zhang, H. Yu, Electrochem. commun. 16 (2012) 73–76.
[52] X.C. Liu, G.C. Wang, R.P. Liang, L. Shi, J.D. Qiu, J. Mater. Chem. A Mater. Energy Sustain. 1 (2013) 3945–3953.
[53] M. Gong, Z. Deng, D. Xiao, L. Han, T. Zhao, Y. Lu, T. Shen, X. Liu, R. Lin, T. Huang, G. Zhou, H. Xin, D. Wang, ACS Catal. 9 (2019) 4488–4494.
[54] C. Qin, A. Fan, X. Zhang, X. Dai, H. Sun, D. Ren, Z. Dong, Y. Wang, C. Luan, J.Y. Ye, S.G. Sun, Nanoscale 11 (2019) 9061–9075.
[55] M.A. Matin, E. Lee, H. Kim, W.S. Yoon, Y.U. Kwon, J. Mater. Chem. A Mater. Energy Sustain. 3 (2015) 17154–17164.
[56] C.Z. Li, Z.B. Wang, X.L. Sui, L.M. Zhang, D.M. Gu, Carbon 93 (2015) 105–115.
[57] L. Zhang, A. Gao, Y. Liu, Y. Wang, J. Ma, Electrochim. Acta 132 (2014) 416–422.
[58] L. Guo, S. Chen, L. Li, Z.A. Wei, J. Power Sources 247 (2014) 360–364.
[59] Y. Wang, H. Zhuo, H. Sun, X. Zhang, X. Dai, C. Luan, C. Qin, H. Zhao, J. Li, M. Wang, J.Y. Ye, S.G. Sun, ACS Catal. 9 (2019) 442–455.
[60] L.F. Shen, B.A. Lu, X.M. Qu, J.Y. Ye, J.M. Zhang, S.H. Yin, Q.H. Wu, R.X. Wang, S.Y. Shen, T. Sheng, Y.X. Jiang, S.G. Sun, Nano Energy 62 (2019) 601–609.
[61] P. Chen, H. Wu, T. Yuan, Z. Zou, H. Zhang, J. Zheng, H. Yang, J. Power Sources 255 (2014) 70–75.
[62] Q. Huang, J. Jiang, J. Chai, T. Yuan, H. Zhang, Z. Zou, X. Zhang, H. Yang, J. Power Sources 262 (2014) 213–218.
[63] V. Baglio, D. Sebastián, C. D'Urso, A. Stassi, R.S. Amin, K.M. El-Khatib, A.S. Aricò, Electrochim. Acta 128 (2014) 304–310.
[64] S. Chen, F. Ye, W. Lin, Int. J. Hygrogen Energy 35 (2010) 8225–8233.